Reconstruction of three-dimensional porous media using a single thin section

Pejman Tahmasebi[1] and Muhammad Sahimi[2,*]

[1]*Department of Mining, Metallurgy and Petroleum Engineering, Amir Kabir University of Technology, Tehran 15875-4413, Iran*

[2]*Mork Family Department of Chemical Engineering & Materials Science, University of Southern California, Los Angeles, California 90089-1211, USA*

(Received 10 March 2012; published 29 June 2012)

The purpose of any reconstruction method is to generate realizations of two- or multiphase disordered media that honor limited data for them, with the hope that the realizations provide accurate predictions for those properties of the media for which there are no data available, or their measurement is difficult. An important example of such stochastic systems is porous media for which the reconstruction technique must accurately represent their morphology—the connectivity and geometry—as well as their flow and transport properties. Many of the current reconstruction methods are based on low-order statistical descriptors that fail to provide accurate information on the properties of heterogeneous porous media. On the other hand, due to the availability of high resolution two-dimensional (2D) images of thin sections of a porous medium, and at the same time, the high cost, computational difficulties, and even unavailability of complete 3D images, the problem of reconstructing porous media from 2D thin sections remains an outstanding unsolved problem. We present a method based on multiple-point statistics in which *a single* 2D thin section of a porous medium, represented by a digitized image, is used to reconstruct the 3D porous medium to which the thin section belongs. The method utilizes a 1D raster path for inspecting the digitized image, and combines it with a cross-correlation function, a grid splitting technique for deciding the resolution of the computational grid used in the reconstruction, and the Shannon entropy as a measure of the heterogeneity of the porous sample, in order to reconstruct the 3D medium. It also utilizes an adaptive technique for identifying the locations and optimal number of hard (quantitative) data points that one can use in the reconstruction process. The method is tested on high resolution images for Berea sandstone and a carbonate rock sample, and the results are compared with the data. To make the comparison quantitative, two sets of statistical tests consisting of the autocorrelation function, histogram matching of the local coordination numbers, the pore and throat size distributions, multiple-points connectivity, and single- and two-phase flow permeabilities are used. The comparison indicates that the proposed method reproduces the long-range connectivity of the porous media, with the computed properties being in good agreement with the data for both porous samples. The computational efficiency of the method is also demonstrated.

DOI: 10.1103/PhysRevE.85.066709 PACS number(s): 02.70.−c, 81.05.Rm, 47.56.+r

I. INTRODUCTION

Flow and transport properties of porous media are controlled by the morphology of their pore space, namely, the geometry—the shapes and sizes of the pores—and the connectivity—the way the pores are connected and the frequency of their interconnection [1–3]. Estimating such properties requires, as the first step, accurate representation of the pore space. Advances in instrumentations, such as laser scanning confocal microscopy [4], serial sectioning [5], x-ray computed microtomography (micro-CT) [6–10], focused ion beams [11], and magnetic resonance computed microtomography [7], have made it possible to obtain three-dimensional (3D) images of porous media. Due to a variety of factors, however, such as the unavailability of the instruments, and their relatively low resolution and the high cost, the application of such methods has not become widespread. On the other hand, in contrast to 3D images, high resolution 2D sections of porous media can be obtained with relative ease. One way of developing a model of a porous medium is by *reconstruction* [2,3]: given a certain amount of data and information about the medium, one attempts to generate realizations of the porous medium that honor the data, with the hope that the reconstructed model provides accurate predictions for those properties of the pore space for which no data are available, or their measurement is difficult and costly. Over the past two decades several methods have been developed for reconstruction of 3D porous media. Generally speaking, such methods may be divided into two groups.

In one group are what we refer to as *stochastic reconstruction* methods. Most of such methods use some sort of correlation functions, obtained from 2D thin sections, to reconstruct 3D porous medium [12–16]. Typically, such reconstruction techniques [17–20], as well as some of those described below, are based on an optimization technique such as, for example, simulated annealing [21] or the genetic algorithm [22], whereby one tries to minimize the difference between the data and the simulated (reconstructed) model using the optimization techniques. The constraints (data) that were used in the first of such techniques were mostly based on two-points statistics that are too simple and cannot, in general, reproduce accurately the variability and connectivity of the pore space [10,19,23,24].

*Corresponding author: moe@usc.edu

In the second group are what we refer to as the *process-based reconstruction* methods, whereby one tries to mimic the processes that gave rise to the present rock and porous media. The approach [25,26] is appealing, but has certain limitations that were addressed later by others [27]. For example, the require very large computer memory, and the required computations are very intensive. In addition, being based on the actual physical processes, such models are not general enough, as they are developed for specific types of porous media. For example, process-based reconstruction methods have been developed for sandstone and carbonate rock with various degrees of success [28–30].

To improve the stochastic reconstruction techniques, use of other types of two-point correlation functions and statistics has been proposed. Such statistics include lineal-length [9,18,31–36] and chord-length distributions [19,24,37–40], which represent, respectively, the probability of finding a line of a given length fully in the pore or grain section, and that of the length between two grain voxels for a specific direction. Clearly, it is possible to increase the quality and accuracy of the reconstruction techniques by adding higher-order statistical measures. But, doing so increases the computation time dramatically. In addition, measurement of high-order statistics of disordered porous media is very difficult.

Almost all the aforementioned reconstruction methods have the shortcoming that they cannot reproduce correctly the connectivity of the matrix and the pore space. To our knowledge, the first attempt to rectify this was that of Hamzepour *et al.* [41]. They showed that if dynamic data, such as single-phase fluid flow data that clearly depend on the connectivity of the pore space, are included in the reconstruction method, not only can the reconstructed model honor the data, but also provide accurate predictions for two-phase flow properties of the same pore space, which depend sensitively on the connectivity, even if no data for such properties are included in the reconstruction process. More recently, a two-point cluster function, which is sensitive to the topological connectivity of the spatial distribution of the phases within a multiphase system, was proposed and used by Torquato and co-workers [42] that also improved the accuracy of the reconstructed systems that they studied.

A promising technique to reconstruct disordered porous media is the method of multiple-point statistics (MPS). Several of such methods have been introduced in the literature on mathematical geology. A comprehensive review of the current MPS methods is given by Tahmasebi *et al.* [43]. In particular, a promising MPS method was introduced by Strebelle [44], usually referred to as the single normal equation simulation (SNESIM). Okabe and Blunt [45] used the method to reconstruct porous media. The connectivity of the reconstructed models turned out to be more accurate than those reconstructed by two-point statistics and various correlation functions. The method requires, however, very demanding computations, and also has difficulty reconstructing anisotropic porous media that are, however, prevalent in practice, particularly in geological formations. More recently, Hajizadeh *et al.* [46] used a multiscale variation of the MPS method, which partially overcame the limitations of the MPS method of Okabe and Blunt [45].

In addition to its computational intensity, the MPS-SNESIM algorithm, though promising, has several shortcomings. One is that it requires very large computer memory. Another problem is that the method usually fails if the medium is highly heterogeneous, because in the MPS-SNESIM method the data are stored in a search tree, but only the local patterns of, or data for the medium that occur frequently enough in the image, are stored. Thus, if a pattern is not repeated often enough, the method deletes it from the image and repeats the search. Such a reduction in the data leads the algorithm to fail reproducing the large-scale connectivity of large-scale porous media that are replete with rare events, i.e., patterns of local variations in the properties that are repeated infrequently throughout the pore space.

In this paper we present a MPS algorithm for reconstruction that we refer to as the cross-correlation–based simulation (CCSIM). The method is used to reconstruct 3D porous media using *a single* 2D thin section. We demonstrate that the reconstruction method possesses several desirable properties, including low computational cost, the ability to generate multiple highly accurate realizations of a pore space, and to reconstruct nonstationary digitized images. The performance of the method is demonstrated with two examples, and the results are compared with the data.

The rest of this paper is organized as follows. In Sec. II the CCSIM algorithm is described. Section III presents the grid splitting and porous media reconstruction algorithm that utilizes the CCSIM method. Section IV describes the results, including the demonstration of the efficiency of the proposed algorithm. The paper is summarized in Sec. V.

II. CCSIM METHOD

Similar to any MPS method, the CCSIM may also be used in two distinct cases, namely, unconditional and conditional simulations that are described below. But, let us first describe the general formulation of the CCSIM, regardless of its type.

A. Cross-correlation function

We first define the notations that are used throughout the paper. The data are represented by a digitized image but, for the sake of convenience, we only use image to refer to it. The patterns in the image are used in order to reconstruct a porous medium. Let us refer to the available data in a specific template $\mathbf{T}$ at location $\mathbf{u}$ as a *data event*, and denote it by $D_T(\mathbf{u})$. $\mathbf{G}$ denotes the computational grid used in the simulation. The template by which the image is scanned is denoted by $\mathbf{T}$, and $D_T^h(\mathbf{u})$ represents the hard—quantitative—data event. Finally, the overlap region between the D_T and the previously simulated pattern is denoted by O (see below).

The main strategy in the CCSIM is using a one-dimensional (1D) raster path, instead of a 2D or 3D random path, used in the previous MPS methods. To accelerate the simulation, we do not use all the data in D_T, but consider the O regions that help us preserve the continuity of the patterns at the boundaries between various regions of the image. We utilize a CC function along a raster path and, as described below, combine it with efficient strategies to honor the continuity and

pattern reproducibility to generate realizations of the porous medium that match the image.

Suppose that $\mathrm{D}(x,y)$ represents the datum at point (x,y) of the image of size $L_x \times L_y$, with $x \in \{0,\ldots,L_x-1\}$ and $y \in \{0,\ldots,L_y-1\}$. We scan the image, focusing on a portion $D_T(\mathbf{u})$ with a size $\ell_x \times \ell_y$, and generate it based on the data such that it matches the corresponding portion in the image. To do so we use a CC function to quantify the similarity between the image and D_T. It is defined by [47]

$$\mathcal{C}(i,j) = \sum_{x=0}^{\ell_x-1}\sum_{y=0}^{\ell_y-1} \mathrm{D}(x+i,y+j)D_T(x,y), \tag{1}$$

where i and j represent the shift steps in the x and y directions, with $0 \leqslant i < L_x+\ell_x-1$ and $0 \leqslant j < L_y+\ell_y-1$. The CC function may also be normalized:

$$\mathcal{C}_N(i,j) = \frac{\sum_{x=0}^{\ell_x-1}\sum_{y=0}^{\ell_y-1}\{[\mathrm{D}(x-i,y-j)-\langle \mathrm{D}_{i,j}\rangle][D_T(x,y)-\langle D_T\rangle]\}^2}{\left\{\left(\sum_{x=0}^{\ell_x-1}\sum_{y=0}^{\ell_y-1}[\mathrm{D}(x-i,y-j)-\langle \mathrm{D}_{i,j}\rangle]^2\right)\left(\sum_{x=0}^{\ell_x-1}\sum_{y=0}^{\ell_y-1}[D_T(x,y)-\langle D_T\rangle]^2\right)\right\}^{1/2}}. \tag{2}$$

Here, $\langle \mathrm{D}_{i,j}\rangle$ is the local mean of $\mathrm{D}(x,y)$ over the D_T segment, shifted to (i,j):

$$\langle \mathrm{D}_{i,j}\rangle = \frac{1}{\ell_x\ell_y}\sum_{x=i}^{i+\ell_x-1}\sum_{y=j}^{j+\ell_y-1}\mathrm{D}(x,y). \tag{3}$$

In a similar fashion $\langle D_T\rangle$, the local mean of D_T, is defined. Equations (1) and (2) indicate that the desired position of (i,j)—the best match with the corresponding point in the image—is one that maximizes $\mathcal{C}(i,j)$ or $\mathcal{C}_N(i,j)$. The normalized CC is less sensitive to changes in the illumination that is not related to a porous medium's image. Due to its simplicity and smaller computational cost, we used Eq. (1). If an image for a heterogeneous porous medium is too complex, the use of $\mathcal{C}(i,j)$ is most appropriate [48], because it produces results that preserve the global variations and continuity of the image (see below).

B. Unconditional reconstruction

By unconditional reconstruction we mean one in which the reconstructed realization does not have to honor *exactly* specific hard data in the image. The raster paths that we utilize have been also used in the past [49], and yielded accurate results in some cases. A problem with the previous applications was, however, preserving the continuity of the porous medium's image in the sectors for which hard data were available. Figure 1 presents the main concepts that we develop in this paper, while its implementation is summarized in Fig. 2. The algorithm begins at the origin of the computational grid **G** (region I in Fig. 1) and proceeds along a raster path on **G**. Since the reconstruction is unconditional, at the beginning **G** is completely empty, containing no hard data. A random patch equal to **T** is selected and inserted into the first D_T, which is then used along an axis (horizontal axis in Fig. 1) along the raster path. One then attempts to locate a patch that matches its left-side overlap, O_l. The O_l region is defined to preserve the continuity near the boundaries and to generate a seamless realization. It is illustrated in Fig. 3, and is the only section comparable with the image. Thus we ignore the rest of the D_T. Recall, as shown in Fig. 3(a), that the aim is to determine the best matched pattern whose left section is correlated with O_l. If, however, several patterns have the same degree of correlations with O_l (the same level of similarity), one of them is selected at random. The procedure continues until inspecting the first line of the raster path is finished, i.e., the algorithm reaches Sec. III in Fig. 1. It then moves forward along and beside the first replaced patch (segment IV in Fig. 1). At that point either the first pattern is not selected randomly, or it has the O_l region on its left side by which the patch is identified; see Fig. 3(b). Next, the algorithm enters a more complex section—segment V in Fig. 1— which is one in which the data event D_T has two overlap regions, O_d at the bottom

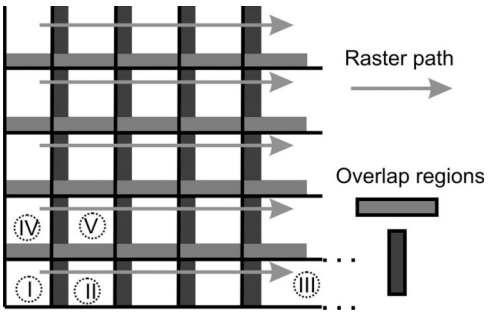

FIG. 1. Example of the raster path and the overlaps regions.

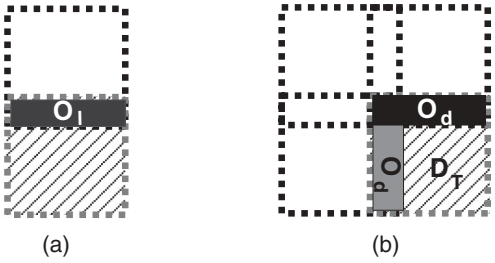

FIG. 2. Three overlap regions that may be created in the simulations with the raster path, with the overlap region that corresponds to (a) the left-side region and (b) the reconstruction that involves the internal nodes.

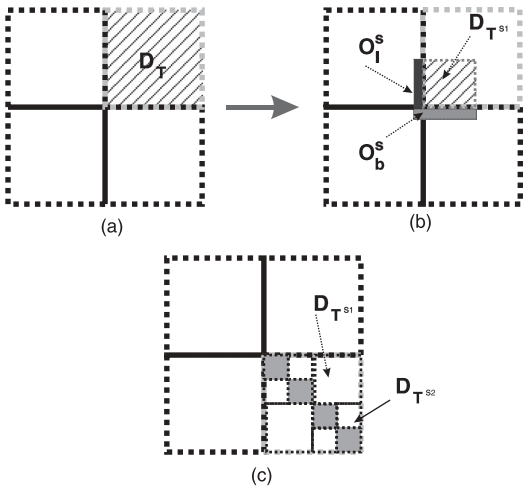

FIG. 3. Adaptive recursive template splitting for the CCSIM. The overlap regions, shown by the shaded gray, are for (a) the prototype of CCSIM without any splitting, (b) when the D_T is split into four sections D_T^{s1}, each of which is simulated separately, and (c) when no matching pattern is found, and D_T^{s1} is split into four equal smaller sections D_T^{s2}.

and on the left side. Therefore, such regions are considered in order to identify the matched pattern; see Fig. 3(c). Thus the algorithm for unconditional reconstruction is as follows.

(i) One defines a raster path on the initial grid **G** according to a given template **T** and overlap region O.

(ii) At each visited node of **G**, one extracts the D_T that consists of new nodes (of the computational grid) and the O region:

(a) One separates the O from D_T and uses it to calculate the CC function.

(b) A new image is determined for comparing the similarities between the O region and the image, based on *both* the CC function and visualization.

(iii) Based on Eq. (1) and an acceptance threshold δ for the O region, one determines the matched pattern. An acceptance threshold $\delta = 0$ implies that the error in the similarity between the O region of the current pattern and the original one is zero. $\delta > 0$ generates an *ensemble of patterns* that do not exactly match the image. In that case one selects a realization at random.

(iv) The selected matched pattern is assigned to the D_T region.

(v) The algorithm moves to another node based on the given parameters on the raster path and repeats the procedures until all nodes of **G** have been visited and inspected, as described above.

In the simulations that were carried out (see below), we used $\delta = 0.2$.

C. Conditional reconstruction

In conditional reconstruction the initial computational grid **G** contains some hard data, which help generate a realization of a porous medium with less uncertainty and a more accurate structure. Conditioning to the hard data and, consequently, the hard data event D_T^h, requires certain changes in the algorithm for unconditional reconstruction, because the matched pattern must honor the hard data, in addition to preserving the continuity of the image. Thus one difference between the algorithms for unconditional and conditional reconstruction is that the latter involves a two-step searching. The first lookup identifies the patterns that honor hard data, while the second step tries to match D_T. Thus the algorithm first computes the CC functions in a manner similar to that for the unconditional case and, according to an acceptance threshold δ, reexamines them and the corresponding patterns.

Those that honor the hard data are identified, and one of them is selected at random and inserted in the D_T^h. If D_T^h is empty, the algorithm proceeds as in the case of unconditional CCSIM. If, however, it is not totally empty, at least one pattern may be identified that honors the hard data and matches the image. A problem may arise when the template **T** is very large, or if the generated realization is not informative enough to honor the hard data, which can lead to discontinuities in the reconstructed medium and prevent the algorithm from identifying a pattern in the ensemble of the realizations that honor the hard data. Such a situation, which arises very rarely, can be addressed rather straightforwardly, due to the intrinsic features of the CCSIM algorithm.

One solution is to increase the threshold δ. In this case, new patterns that have more significant differences with the O region become candidates for inclusion in the ensemble of the possible patterns. δ may be raised until a proper pattern is identified and inserted in D_T^h. But, increasing δ also allows the incorrect patterns to enter the ensemble, which may subsequently lead to the generation of a poor realization of a porous medium that contains discontinuity. To overcome the problem, we may use another raster path in a different direction to improve the quality of the realizations. An alternative approach is to use an adaptive simulation that is shown schematically in Fig. 3. First, the patterns that honor the hard data with the initial threshold δ are identified. If, however, no such pattern is found, the sector D_T is split into smaller data events D_T^s and the reconstruction continues with D_T^s. The splitting continues until the ensemble of the patterns that honor the hard data has at least one member. If the porous medium is anisotropic (stratified), one proceeds as follows. The image is first analyzed to determine the anisotropy direction. The template is then shrunk or expanded in the anisotropy direction. The rest of the reconstruction method is similar to that for isotropic media.

Calculation of the CC function can be carried out in both the spatial and Fourier domains. If the size of the image is not too large, all the computations are carried out in the spatial domain, as is done in the present paper. We will demonstrate in a future paper that very significant savings in computation time is achieved by computing the CC function in the Fourier space, when the image is very large and contains millions of grid blocks.

III. ALGORITHMS

A main idea of the proposed methodology is to use *a single* 2D section of a porous medium, which is obtained from, for example, x-ray micro-CT and utilize it as the foundation—as the image—for reconstruction of the 3D medium. The 2D thin

section represents the first layer for which the next layer is constructed and added to the evolving reconstructing medium, based on the extracted hard data in the previous layer. Then, the newly reconstructed layer acts as the new source of the hard data for the next layer. This strategy reproduces very well the continuity of the porous medium in the direction of layer addition, since each layer has similarities with the previous layer. One may also use the image of layer n as the image for layer $n + 1$, although this might encounter some difficulties, if the porous medium is highly disordered.

For example, any possible artifact in the previous layer may be transferred hierarchically to the following layers. To prevent this from occurring, we use a single image that is representative of the microstructure of all the layers, which is possible if the porous medium is stationary. The following important questions then arise. (1) How should one select the hard data? (2) How many hard data points should one select for the next 2D section? (3) Where (in the image) should one pick the hard data? In addressing such questions two points must be kept in mind. If a large number of hard data points are used, then the next layer or 2D section will be very similar to the previous layer and, thus, the heterogeneity may not be reproduced. On the other hand, if only a few hard data points are used for the reconstruction of the next thin section, the continuity will be lost and the layers will appear to be independent of each other. Therefore, using an optimal number of the hard data points and their spatial locations is an issue that must be addressed.

A. Grid splitting

The hard data points are selected such that the pore and grain phases do not undergo sudden changes, so as to preserve the connectivity of the sample as more layers are added. Therefore, the sampling strategy is neither fully random nor completely deterministic. The most suitable of such strategies is a *multiscale* sampling by which the "best" locations for the sampling are identified such that not only are the shape and states of the pores preserved, but also the pores can be extended to the next layer, or close. This is achieved by a nonuniform or adaptive sampling, called *quadtrees*, which partitions the image into some subsections according to a set criterion. The criterion used in the algorithm is the *entropy* S by which we decide to continue or stop the partitioning. The entropy is a statistical measure of the heterogeneity or stochasticity of the patterns in the image. In other words, to each of the patterns resulting from each partition is assigned an entropy that, given the heterogeneity of the pore space, is a stochastic variable. Then, the histogram of such entropies is constructed and used as for a probabilistic selection. In this study the Shannon entropy [50] is used as a criterion by which we partition the image into some segments (subgrids) that enable us to select the proper samples that convey the variability of the connectivity of the image in all the directions. The Shannon entropy S is computed based on the probability p_i of having states i in the image,

$$S = \sum_{i=1}^{n} p_i \ln p_i, \tag{4}$$

TABLE I. The splitting algorithm.

function $GS \rightarrow$ Grid Splitting (I_m, $b_{\min}$, ζ, Re)

```
1  Calculate the grain and pore proportions;
2  p ← the proportion of the pores in the image (or layer), and
   g ← 1 − p (the grain proportion);
3  I_m ← Input image;
4  b_min ← Minimum size of the blocks;
5  ζ ← Threshold entropy;
6  Re ← Proportion of the hard data is extracted;
7  Hard data are inserted in their locations;
8  Divide the image into four blocks;
9  for each block 1 to 4 do
10  if size (block) > b_min do
11  Calculate Ŝ;
12   if Ŝ > ζ do
13     Divide the block into four blocks;
14   else fix the block size; select Re% of the points in the block
   randomly and add to the hard data;
15    end (for else in 14)
16   end (for if in 12)
17  else fix the block and select one of the nodes as hard data;
18 end (for if in 10)
19  end (for loop in 10)
20 according to p and g select the hard data for conditioning
```

in which n is the number of pixels in the block of the image that we are considering, and p_i is the probability of having the ith pixel in the image. Each pixel is considered as a data point. Thus, for different bins we determine the frequencies of the pixels and compute their histogram. p_i is then given by

$$p_i = (\text{histogram of sample } i)/(\text{length of the sample}).$$

Normalizing the entropies by their maximum value yields the normalized entropies $\hat{S}$. A large $\hat{S}$ is indicative of high complexity or heterogeneity of the image.

The Shannon entropy is not by itself enough for deciding the extent of the partitioning of the grid. We also use a quadtree-based partitioning based on the Shannon entropy. Such an adaptive technique makes it possible to pick the samples very efficiently and "carry" the spatial variability to the next layer. Therefore, if a block meets the criterion, i.e., its normalized entropy is smaller than a threshold entropy ζ, it is homogeneous enough that it need not be divided any further. If, on the other hand, the block's normalized entropy exceeds ζ, it is divided into four blocks and the new smaller blocks are also compared based on their own entropies and whether they exceed the set threshold. The structure of the splitting algorithm is given in Table I, and an example is presented in Fig. 4. A physical constraint that is imposed is that we are not allowed to generate a pore or grain proportion (volume fraction) that is larger than that of the image.

B. Reconstruction algorithm

To refine the algorithm further, we use a strategy called *frame instruction*. Before reconstructing the layers, we construct four frames for the front, right, back, and left sides of the 3D grid, which preserve the continuity of the porous medium in its exterior view and constrain it near the boundaries. Thus

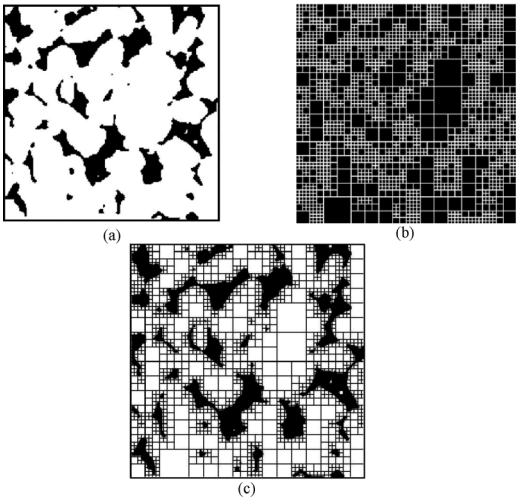

FIG. 4. (a) Original image, (b) the representation of (a) by quadtree decomposition, and (c) the superposition of (a) and (b).

the front layer of the 3D grid, conditioned to an overlap band with the image, is constructed. Then, the right side of the 3D porous medium, conditioned to the front and the image, is constructed. The procedure continues for the remaining two sides of the computational grid. Figure 5 illustrates the procedure schematically. Once the porous medium's frame is constructed, the reconstruction commences.

First, the algorithm determines the optimal locations of the hard data according to the algorithm shown in Table I. In each layer the edges are conditioned to the front, right, back, and left sides to preserve their continuity. Then, according to the extracted hard data and by implementing the CCSIM algorithm, a new layer is reconstructed. The threshold ζ that

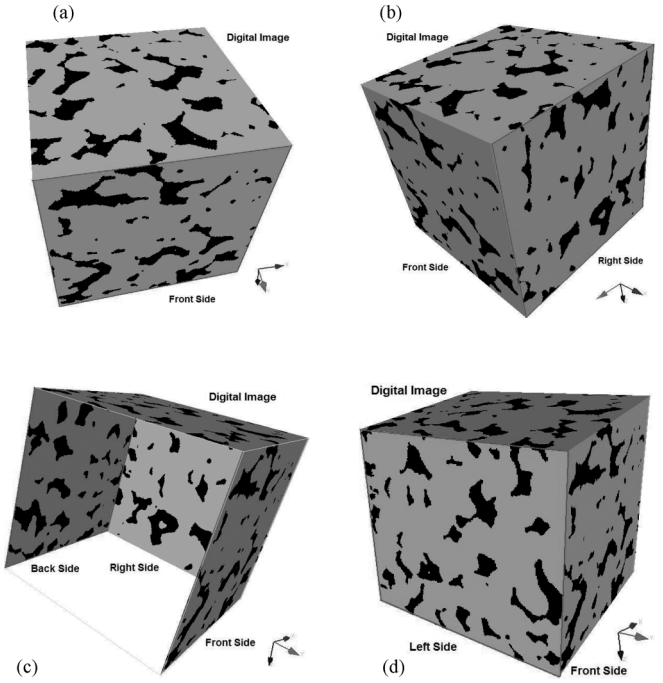

FIG. 5. Four initial steps for constructing the external view of the Berea sandstone.

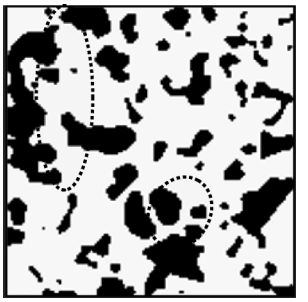

FIG. 6. 2D section of the carbonate rock used as the image. The regions encircled by the ellipses correspond to those in Fig. 8.

we used for the normalized entropies (see Table I) was $\zeta = 0.5$. The procedure continues until all the layers of the given grid are reconstructed. Finally, the reconstructed layers are stacked together to complete the reconstruction of the 3D porous medium.

IV. RESULTS AND DISCUSSION

We selected two sample porous media for reconstruction, the carbonate rock presented by Okabe and Blunt [45], and a Berea sandstone from the group at Imperial College of London [51]. Therefore, a comparison of our results, in terms of both the computation time and the quality of the reconstructed samples, with the previous efforts is also made.

A. Carbonate rock

The carbonate porous sample consists of limestone, and is classified as bioclastic packstone or grainstone [45]; see Fig. 6. It exhibits a variable local porosity ranging from 0.25 to 0.4. We did not have access to the complete original 3D sample, but only the 2D image presented [45]. But, on the other hand, the reconstruction procedure is also based on a single 2D image. A template size of 35×35 and an overlap region O of size of 5 were used in the reconstruction of the sample.

B. Berea sandstone

The 2D section of the sample Berea sandstone used as the image is shown in Fig. 7. It has a size of 200×200 pixels. The sample does not exhibit much variability, with the one used used in the reconstruction having a porosity of 0.2, compared with the porosity of 0.22 for the 3D sample. Therefore, the sample used contains the heterogeneity of the original rock. In

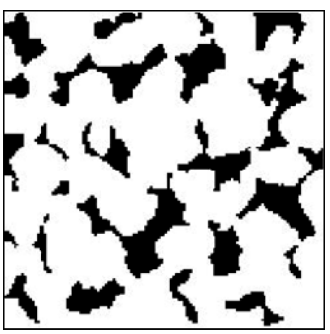

FIG. 7. 2D thin section of the Berea sandstone used as the image.

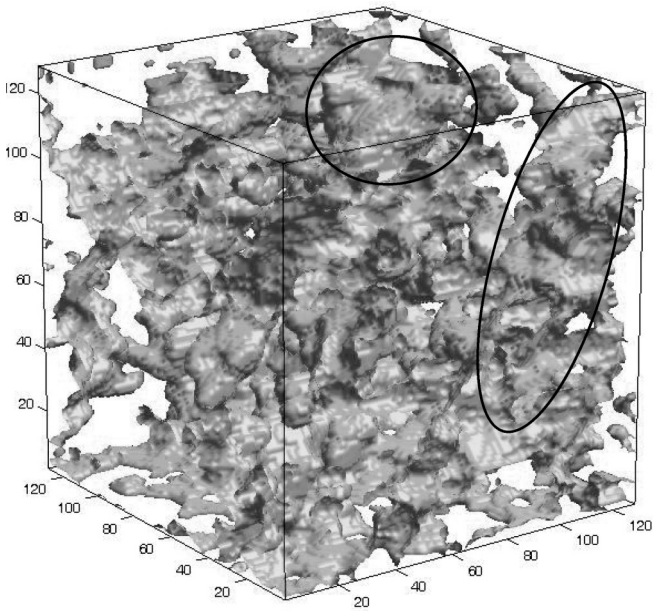

FIG. 8. Reconstructed 3D carbonate rock sample. The regions indicated by the ellipses correspond to those shown in Fig. 6.

this case, an original 3D sample was available with which the reconstructed model can be compared directly. The size of the template **T** used in the reconstruction was 20×20, and that of the O region was 4—weaker heterogeneity requires smaller templates and O regions. Altogether, 5% of the data for both sample porous media was used in the reconstruction.

C. Reconstructed porous media

The reconstructed carbonate porous medium is shown in Fig. 8, which has a size of $200 \times 200 \times 200$ pixels. The complete 3D view, the cross sections and the transparent view of the reconstructed sample are presented in Fig. 9.

The result for the reconstructed Berea sandstone is shown in Fig. 10, where it is compared with the 3D image of the original sample, and in Fig. 11 where the side views of the reconstructed sample are compared with the original data. They indicate that the reconstructed sample has reproduced the structure and connectivity of the original system. Thus, at the visual level, the CCSIM method is capable of preserving the connectivity of the samples in the direction of stacking the 2D images that it reconstructs, as well as the variability in the spatial distribution of the pores.

If the image represents a stationary structure, the proposed algorithm reproduces accurate reconstruction of porous media. But, at the same time, unlike many methods proposed in the past, even a sample with a nonstationary structure can be reconstructed accurately by the proposed method, except that one must use a number of 2D sections that convey the nonstationarity of the sample's properties. Consider, for example, the large and continuous substructures shown by the two ellipsoids in Fig. 6. They are reproduced correctly in Fig. 8, whereas the SNESIM method used by Okabe and Blunt [45] did not reproduce such large structures. At the same time, it should be pointed out that the algorithm of Okabe and Blunt is sensitive to the stationarity of the image. Due to the

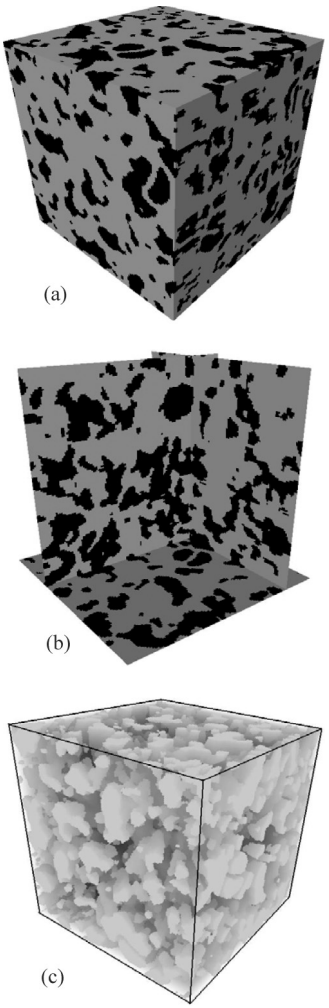

FIG. 9. (a) 3D exterior view of the reconstructed carbonate sample; (b) a cross section of the reconstructed sample, and (c) the transparent view of the porous medium in which the gray color represents the pore space.

flexibility of our algorithm for using a large template **T**, both large- and small-scale structures are reproduced. Moreover, if in the application of the SNESIM one uses a larger template to capture the large-scale structures, the search tree will ignore the small replicas and, as a result, cannot reproduce them accurately. Furthermore, using a large template leads the SNESIM to require large computer memory and will be very demanding computationally. For example, the algorithm by Okabe and Blunt [45] took about 14 CPU hours to reconstruct the sample, whereas our proposed methodology took only about 1.25 CPU hours with a comparable computer, a factor of about 14 faster. In addition to the aforementioned reasons for the differences between the CCSIM and SNESIM, one must also recognize that the latter is a *pixel-based* algorithm that reconstructs one pixel at a time, whereas the former is a *pattern-based* method that reconstructs a large number of points *simultaneously*.

Visual inspection and similarities between the image and the reconstructed media are not sufficient for judging the accuracy of the method. Hence we now present a more

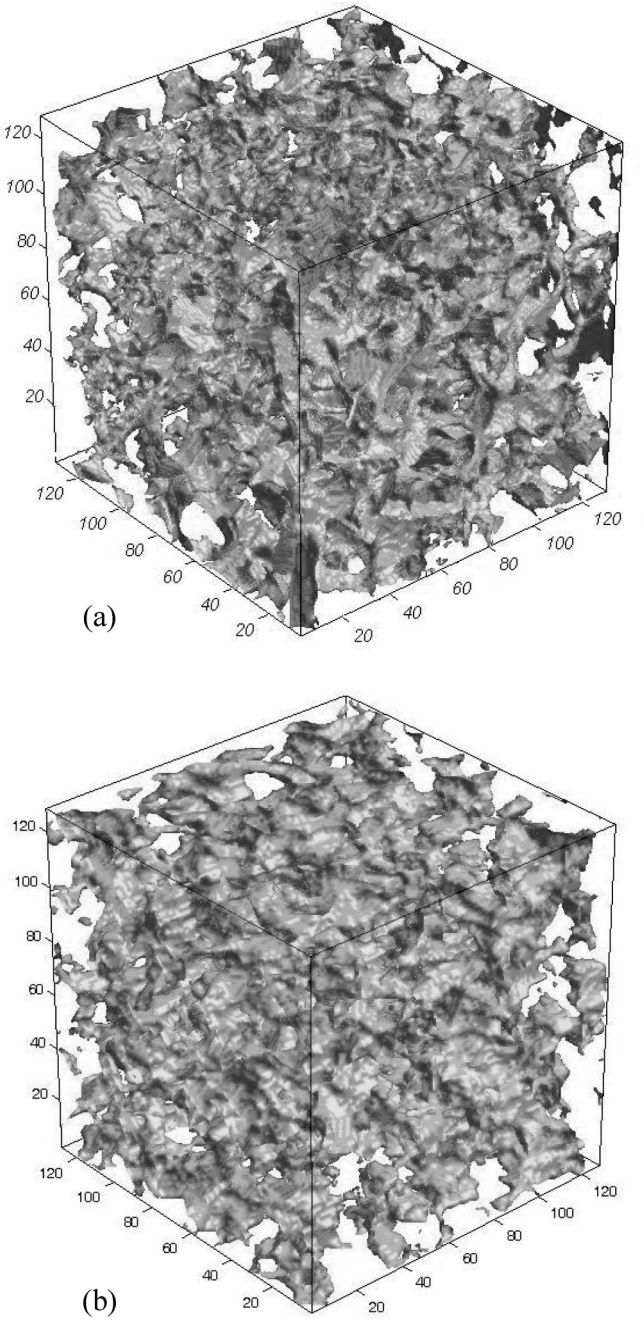

FIG. 10. (a) 3D view of the original Berea sandstone and (b) the reconstructed porous medium.

quantitative comparison between the computed results and those of the image.

D. Autocorrelation function

The void-void (pore-pore) autocorrelation function (ACF) is defined by

$$\mathcal{R}(\mathbf{u}) = \frac{\langle [I(\mathbf{r}) - \phi][I(\mathbf{r}+\mathbf{u}) - \phi] \rangle}{\phi - \phi^2}, \tag{5}$$

where the averaging is over all locations $\mathbf{r}$ within the system, and $I(\mathbf{r})$ is an indicator function, such that $I(\mathbf{r}) = 1$ if $\mathbf{r}$ is in the pore space, and $I(\mathbf{r}) = 0$ otherwise. The porosity is simply $\phi = \langle I(\mathbf{r}) \rangle$. We compare the ACFs of the image, the micro-CT image of the porous media, and the reconstructed carbonate sample, but one must keep in mind that the ACF is not by itself sufficient as a test of the accuracy of the reconstructed media. The ACFs were computed in the three orthogonal directions for the Berea sandstone, for which we had access to the full 3D image, and in two orthogonal directions for the carbonate sample, for which only a 2D image was available. The comparisons for the Berea sandstone and the carbonate sample are presented in Figs. 12 and Fig. 13, respectively.

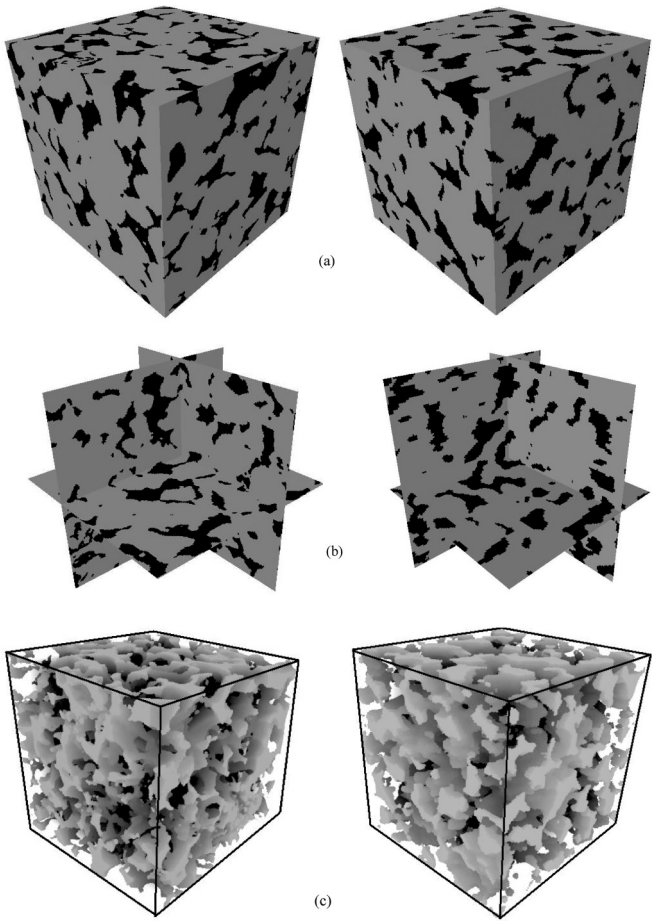

FIG. 11. Results for the reconstructed Berea sandstone (right) and their comparison with original 3D porous medium (left). (a) Full 3D view in which the black areas represent the pores and the gray shows the grains, (b) cross sections of the two porous media, and (c) the transparent view that shows the pores.

It is clear that the ACFs of the reconstructed porous media match the actual data. In particular, the results for Berea sandstone are very accurate.

E. Porosity distribution

The variations of the porosity of various layers of the micro-CT image of the Berea sandstone are compared in Fig. 14 with those in the reconstructed porous medium. The patterns are similar. Moreover, except for a few points, the numerical values of the two porosities are also close everywhere. While

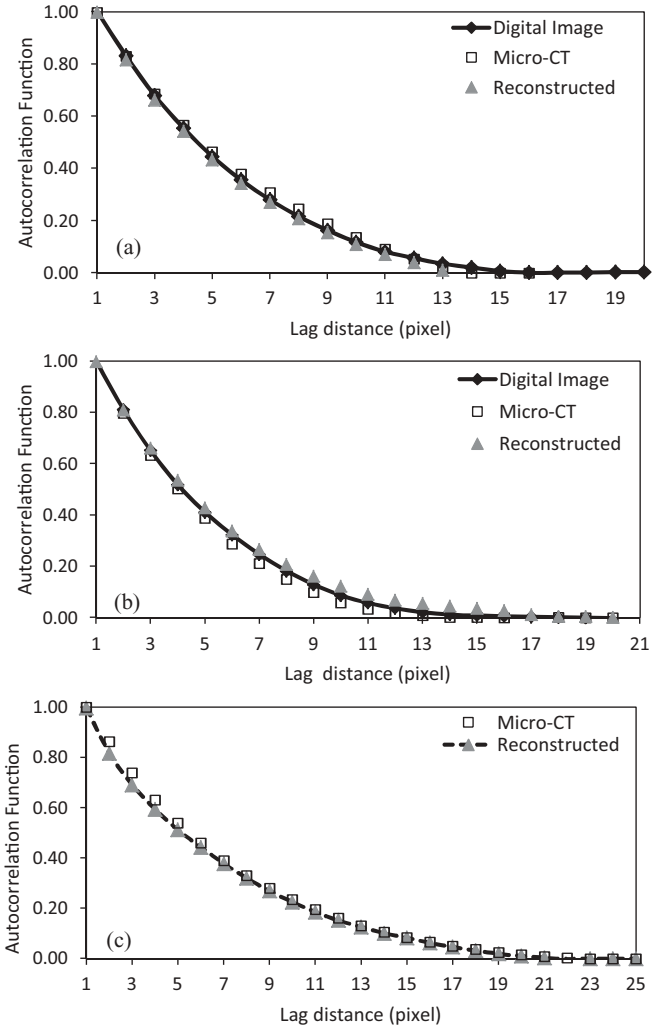

FIG. 12. Comparison of ACFs for three images, in (a) the x (horizontal) direction, (b) the y (vertical) direction, and (c) the z direction (perpendicular to the page). The results are for Berea sandstone.

the porosity does not vary greatly, the similarity of its variation in the reconstructed sample with that of the image is notable.

F. Multiple-point connectivity probability

Multiple-point connectivity is a measure of the connectivity of the system within an image [52]. It is a concept more general than the coordination number that characterizes the *local* connectivity of the pores, and is concerned with determining the probability $p(h;m)$ of having a sequence or a continuous string of m points in a structure in any given direction, such as pores in a pore space. It is defined by

$$p(\mathbf{h};m) = \text{Prob}\{I(\mathbf{u}) = 1, I(\mathbf{u}+\mathbf{h}) = 1, \ldots, I(\mathbf{u}+m\mathbf{h}) = 1\}, \quad (6)$$

where $\mathbf{h}$ is a unit vector in the direction along which $p(\mathbf{h},m)$ is estimated. The advantage of such a connectivity function, in addition to its global nature, is that it allows one to account for curvilinearity of the system by considering a tolerance core

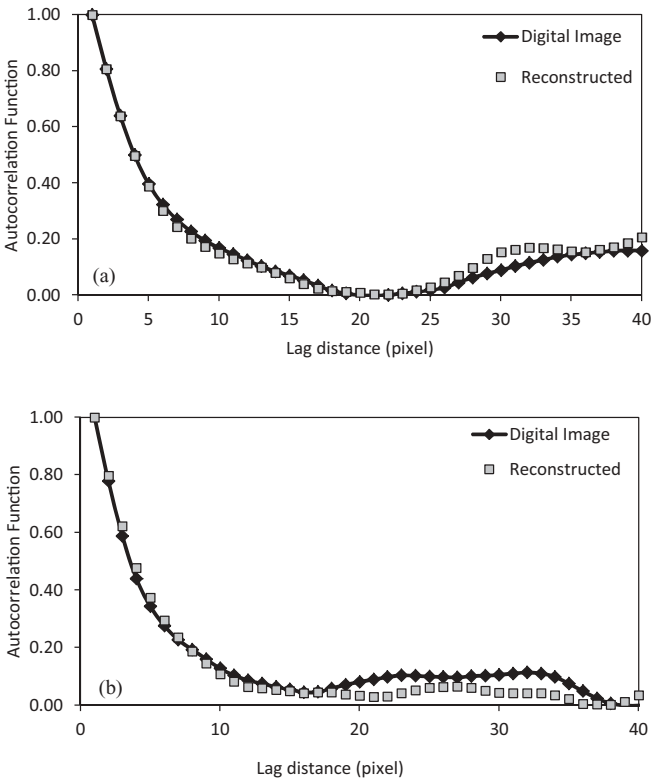

FIG. 13. Comparison of the ACFs for two images, in (a) the x direction and (b) the y direction. The results are for the carbonate sample.

around a target direction. The results for the Berea sandstone in the three orthogonal directions, and for the carbonate sample in two orthogonal directions are shown in Figs. 15 and 16, respectively. Both sets of results indicate the accuracy of the reconstructed models.

G. Single- and two-phase flow characteristics

Although the comparisons made so far indicate the accuracy of the proposed algorithm, they were based on some limited statistics. It is entirely possible for two models to have the similar such statistics, but very different flow characteristics.

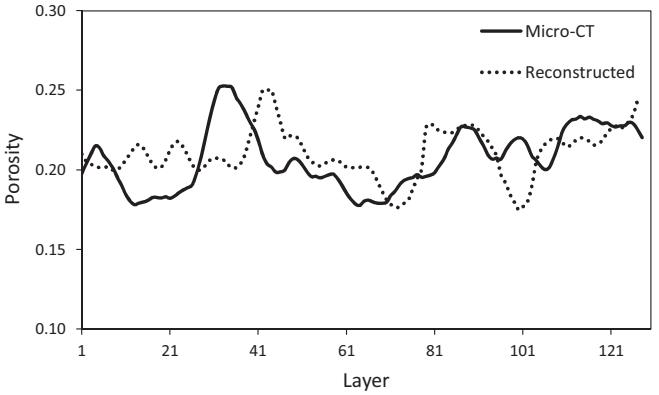

FIG. 14. Comparison of the porosity distribution in the reconstructed Berea sandstone with that of its micro-CT 3D image.

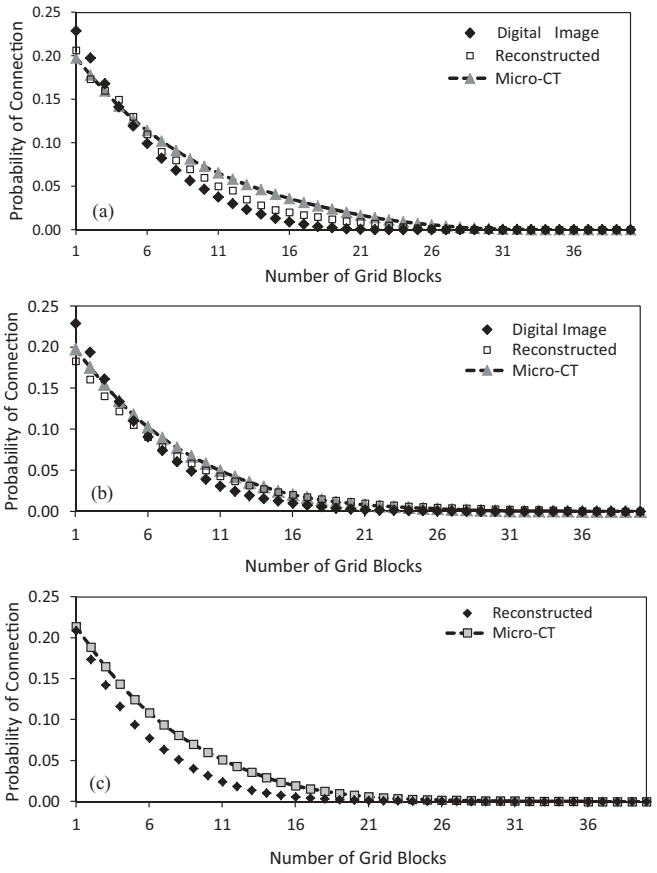

FIG. 15. Comparison of the multiple-point connectivity probability for three images of the Berea sandstone in the (a) x, (b) y, and (c) z directions (see Fig. 12 for the directions).

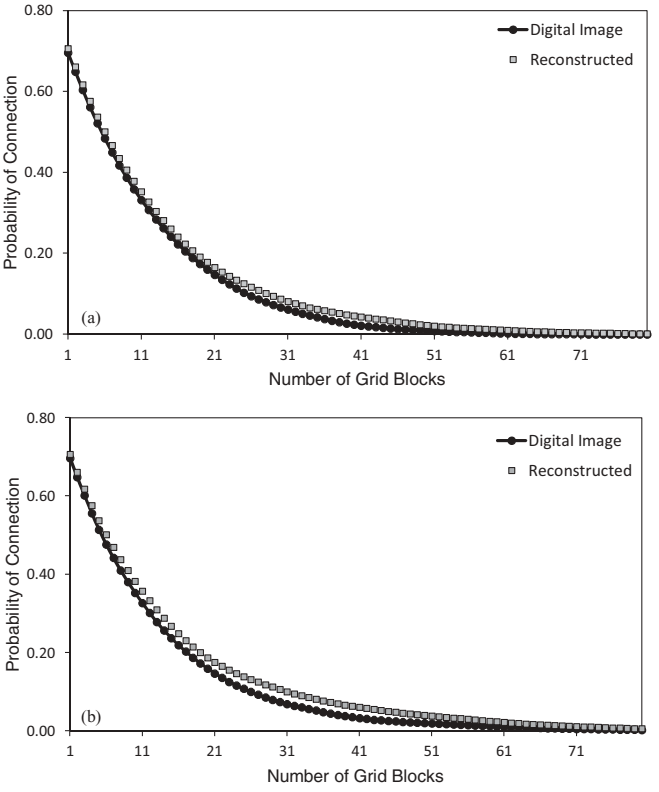

FIG. 16. Same as in Fig. 15, but for the carbonate porous medium, in the (a) x and (b) y directions.

Therefore, in this section we present a comparison between the flow properties of the reconstructed models and those of the image.

We first compare the Darcy permeability for single-phase flow in the porous medium. While, due to the complex structure of the pore space, a technique such as the lattice Boltzmann simulation may be more accurate, we wish to make only a preliminary comparison between the effective permeabilities of the reconstructed porous medium and the image's. Thus the FLOWSIM package [53] was used for the flow simulation and computation of the permeability. A constant pressure gradient was applied across the model in one direction, while no flow boundary conditions were used on the remaining faces. A computational grid of the size of $30 \times 30 \times 30$ was used. The simulator generates the (average) pressure in each grid block and computes the input and output flows (which are equal under steady-state condition). We assumed the permeabilities of the pores and grains to be 100 and 0.01 mD, respectively. Strictly speaking, the latter must, of course, be zero, but we set it to be a small value to avoid numerical difficulties in the simulations. The results for the effective permeabilities K_e of the Berea sandstone in the three orthogonal directions are presented in Table II, indicating reasonable agreement between those for the reconstructed model and those of the original Berea sandstone. But, perhaps the most reliable indicator of the accuracy of the reconstructed porous media is their relative permeabilities (RPs) to two-phase flow through their pore space, because the RPs are sensitive to the connectivity of the pores [3,41]. The RP of a fluid phase is defined as the effective permeability of that part of the pore space occupied by the fluid, divided by the overall single-phase permeability of the pore space.

One way of computing the RPs is by first developing the equivalent pore network model of the porous medium, represented by a network of pores and throats, for which various methods have been proposed [3]. In this work we used the method proposed by Dong and Blunt [54] who used the maximal ball algorithm to extract the sizes of the pores and throats from images of the porous medium. Figure 17 compares the distributions of the local coordination numbers, and the size distributions for the pores and throats in the reconstructed Berea sandstone and its actual 3D image. The two sets of results agree well. Once the network equivalent model was constructed, two-phase flow simulations of oil and water in the Berea sandstone were carried out, using a method similar to that of Valvantne and Blunt [55]. The network size was $200 \times 200 \times 200$, the oil and water density were assumed to be 900 and 1000 kg/m^3, respectively, the water-oil surface tension was taken to be 3×10^{-2} N/m, while the oil and water viscosities were assumed to be 1.2×10^{-3} and 1.0×10^{-3} kg/m s, respectively. We simulated the primary drainage—displacement of a nonwetting phase (oil) by the wetting phase—followed by the reverse imbibition process. The simulator combines the topologically disordered

TABLE II. Comparison of the computed effective permeabilities for the original micro-CT image and the reconstructed Berea sandstone.

	Micro-CT porous media			Reconstructed porous media		
	$K_e\,(x)$	$K_e\,(y)$	$K_e\,(z)$	$K_e\,(x)$	$K_e\,(y)$	$K_e\,(z)$
Max	100	100	100	100	100	100
Upper quartile	100	100	100	100	100	100
Median	100	100	100	93.85	93.65	91.01
Lower quartile	49.38	49.47	51.36	58.89	57.50	43.1
Min	0.1	0.1	0.1	0.1	0.1	0.1
Mean	73.73	73.64	74.23	75.01	74.54	70.12

prenetwork that represents the image and its reconstructed version with detailed two-phase flow displacement mechanisms [3] for any sequence of water and oil flooding, and any wettability of the pores' surface. During the primary flooding the pore network is assumed to be strongly wetted by the wetting phase (water for the water-oil systems and oil for the oil-gas system, or oil in carbonate rock) with a receding contact angle of 0°. During the secondary flooding the advancing contact angles will be larger (than zero), due to roughness of the surface and minor wettability alteration [3].

The computed results for both the reconstructed sample and the original 3D Berea sandstone are presented in Fig. 18. The agreement between the two sets of results is excellent, indicating the accuracy of the reconstructed model.

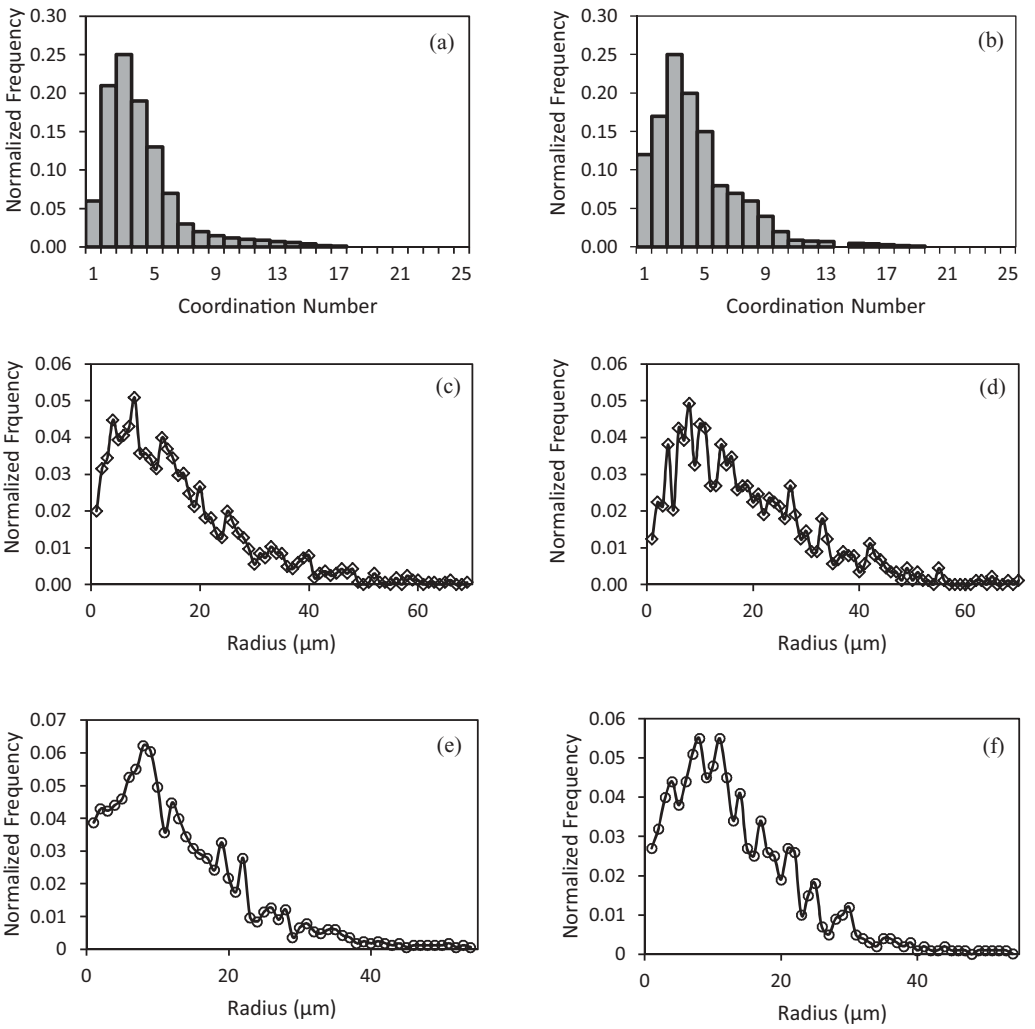

FIG. 17. Distributions of (a) the coordination number, (b) the throat sizes, and (c) the pore sizes for the Berea sandstone. On the left are the results for the original sandstone and on the right for the reconstructed one.

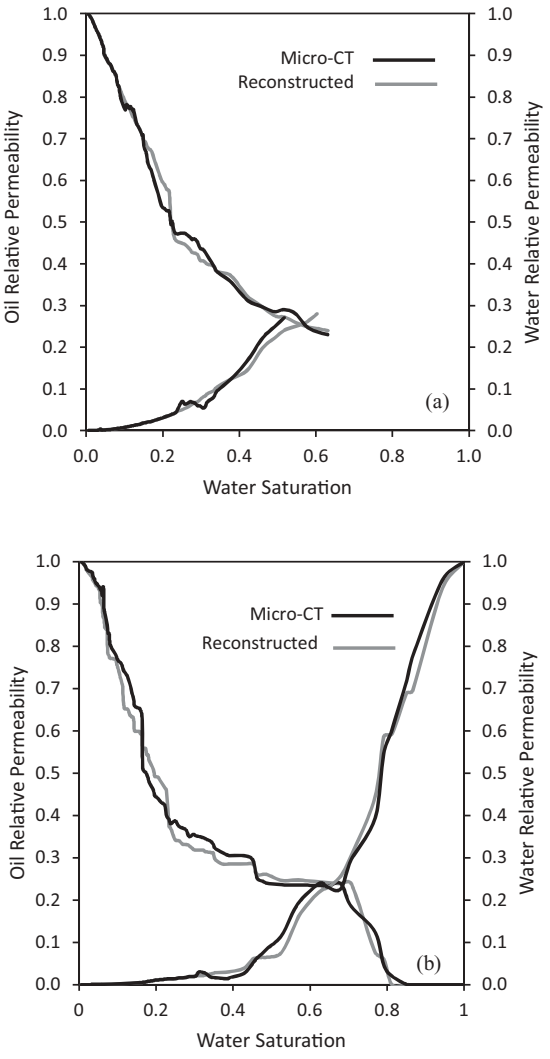

FIG. 18. Comparison of the computed relative permeabilities to the oil and water phases during (a) drainage and (b) imbibition.

V. SUMMARY

We proposed and developed a multiple-point statistic (MPS) method with the goal of reconstructing 3D porous media from *a single* 2D thin section. To preserve the long-range (global) connectivity of the pore space, we utilized a MPS method method based on a cross-correlation function that has been used in image processing. Based on a digitized image of a thin (2D) section of a porous medium, a second thin section is reconstructed, which is then used to reconstruct a third layer, and so on. The reconstructed layers are then stacked together to generate the entire reconstructed 3D porous medium. To do so successfully, a most important issue was addressed, namely, how to select the amount and location of the hard data that are used to constrain the reconstruction. We developed an adaptive grid splitting method based on the entropy of the blocks. A distinct advantage of the method is the possibility of using a large template in the CCSIM method, which allows reconstructing nonstationary images, whereas most of the previous algorithms, and in particular the SNESIM method, are applicable only to stationary images. The method was tested for a Berea sandstone and the 2D image of a carbonate porous sample. The properties of the reconstructed models agreed well with those of the actual samples. Given the computational efficiency of the proposed method, as well as its accuracy, we believe that the algorithm suggested in this paper has potential applications to reconstruction of a wide variety multiphase systems, some of which will be studied and reported in the near future.

ACKNOWLEDGMENTS

Work at USC was supported in part by the Department of Energy. We thank A. Hajizadeh for several useful discussions.

[1] P. M. Adler, *Porous Media: Geometry and Transport* (Butterworth, Boston, 1992).
[2] S. Torquato, *Random Heterogeneous Materials* (Springer, New York, 2002).
[3] M. Sahimi, Rev. Mod. Phys. **65**, 1393 (1993); *Flow and Transport in Porous Media and Fractured Rock*, 2nd ed. (Wiley-VCH, Weinheim, 2011); *Heterogeneous Materials I & II* (Springer, New York, 2003).
[4] J. T. Fredrich, Phys. Chem. Earth A: Solid Earth Geodesy **24**, 551 (1999).
[5] C. Lin and M. H. Cohen, J. Appl. Phys. **53**, 4152 (1982); R. M. Holt, E. Fjaer, O. Torsaeter, and S. Bakke, Marine Pet. Geol. **13**, 383 (1996).
[6] J. H. Dunsmuir, S. R. Ferguson, K. L. D'Amico, and J. P. Stokes, SPE Paper 22860, in Proceedings of the Society of Petroleum Engineers Annual Meeting, Dallas, Texas, 1991 (unpublished).
[7] J. K. Jasti, G. Jesion, and L. Feldkamp, SPE Formation Eval. **8**, 189 (1993).
[8] P. Spanne, J.-F. Thovert, C. J. Jacquin, W. B. Lindquist, K. W. Jones, and P. M. Adler, Phys. Rev. Lett. **73**, 2001 (1994).
[9] D. A. Coker, S. Torquato, and J. H. Dunsmuir, J. Geophys. Res. Solid Earth **101**, 17497 (1996).
[10] M. E. Coles, R. D. Hazlett, E. L. Muegge, K. W. Jones, B. Andrews, B. Dowd, P. Siddons, A. Peskin, P. Spanne, and W. Soll, SPE Reservoir Eval. Eng. **1**, 288 (1998).
[11] H. Ishida, Observation of micro-fabric of source rock by focused ion-beam workstation, Japan National Oil Corporation, 1997 (unpublished); L. Tomutsa and V. Radmilovic, in Proceedings of the International Symposium of the Society of Core Analysts, publication SCA2003-47, 2003 (unpublished).
[12] J. A. Quiblier, J. Colloid Interface Sci. **98**, 84 (1984).
[13] P. M. Adler, C. G. Jacquin, and J. A. Quiblier, Int. J. Multiphase Flow **16**, 691 (1990).

[14] A. P. Roberts, Phys. Rev. E **56**, 3203 (1997).

[15] M. A. Ioannidis, M. J. Kwiecien, and I. Chatzis, Transp. Porous Media **29**, 61 (1997); M. A. Ioannidis, I. Chatzis, and M. J. Kwiecien, J. Canad. Pet. Technol. **38**, 18 (1999); M. A. Ioannidis and I. Chatzis, J. Colloid Interface Sci. **229**, 323 (2000).

[16] Z. R. Liang, C. P. Fernandes, F. S. Magnani, and P. C. Philippi, J. Pet. Sci. Eng. **21**, 273 (1998); Z. R. Liang, P. C. Philippi, C. P. Fernandes, and F. S. Magnani, SPE Reservoir Eval. Eng. **2**, 161 (1999).

[17] C. L. Y. Yeong and S. Torquato, Phys. Rev. E **57**, 495 (1998).

[18] C. L. Y. Yeong and S. Torquato, Phys. Rev. E **58**, 224 (1998).

[19] P. Levitz, Adv. Colloid Interface Sci. **77** (1998).

[20] S. Bekri, K. Xu, F. Yousefian, P. M. Adler, J.-F. Thovert, J. Muller, K. Iden, A. Psyllos, A. K. Stubos, and M. A. Ioannidis, J. Pet. Sci. Eng. **25**, 107 (2000).

[21] S. Kirkpatrick, C. D. Gellat, Jr., and M. P. Vecchi, Science **220**, 671 (1983).

[22] C. R. Reeves and J. E. Rowe, *Genetic Algorithms Principle and Perspectives: A. Guide to GA Theory* (Kluwer Academic, Dordrecht, 2003); R. Sanchez, T. T. Tsotsis, and M. Sahimi, Chem. Eng. Sci. **62**, 6378 (2007); H. Li, R. Sanchez, S. J. Qin, H. I. Kavak, I. A. Webster, T. T. Tsotsis, and M. Sahimi, *ibid.* **66**, 2646 (2011).

[23] R. D. Hazlett, Transp. Porous Media **20**, 21 (1995); Math. Geol. **29**, 801 (1997).

[24] M. E. Kainourgiakis, E. S. Kikkinides, T. A. Steriotis, A. K. Stubos, K. P. Tzevelekos, and N. K. Kanellopoulos, J. Colloid Interface Sci. **231**, 158 (2000); M. E. Kainourgiakis, T. A. Steriotis, E. S. Kikkinides, G. Romanos, and A. K. Stubos, Colloids Surf. A **206**, 321 (2002).

[25] J. N. Roberts and L. M. Schwartz, Phys. Rev. B **31**, 5990 (1985); L. M. Schwartz and S. Kimminau, Geophysics **52**, 1402 (1987).

[26] S. L. Bryant and M. J. Blunt, Phys. Rev. A **46**, 2004 (1992); S. L. Bryant and S. Raikes, Geophysics **60**, 437 (1995); S. L. Bryant, P. R. King, and D. W. Mellor, Transp. Porous Media **11**, 53 (1993); S. L. Bryant, D. W. Mellor, and C. A. Cade, AIChE J. **39**, 387 (1993).

[27] D. Coelho, J.-F. Thovert, and P. M. Adler, Phys. Rev. E **55**, 1959 (1997); J. P. Latham, Y. Lu, and A. Munjiza, Geotechnique **51**, 871 (2001); J. P. Latham, A. Munjiza, and Y. Lu, Powder Technol. **125**, 10 (2002).

[28] S. Bakke and P.-E. Øren, SPE J. **2**, 136 (1997); P.-E. Øren, S. Bakke, and O. J. Arntzen, *ibid.* **3**, 324 (1998); P.-E. Øren and S. Bakke, Transp. Porous Media **46**, 311 (2002); J. Pet. Sci. Eng. **39**, 177 (2003).

[29] B. Biswal and R. Hilfer, Physica A **266**, 307 (1999); B. Biswal, C. Manwart, and R. Hilfer, *ibid.* **273**, 452 (1999); B. Biswal, P.-E. Øren, R. J. Held, S. Bakke, and R. Hilfer, Phys. Rev. E **75**, 061303 (2007).

[30] M. Pilotti, Transp. Porous Media **41**, 359 (2000).

[31] B. Lu and S. Torquato, Phys. Rev. A **45**, 922 (1992); **45**, 7292 (1992).

[32] D. A. Coker and S. Torquato, J. Appl. Phys. **77**, 6087 (1995).

[33] C. Manwart, S. Torquato, and R. Hilfer, Phys. Rev. E **62**, 893 (2000).

[34] I. Hidajat, A. Rastogi, M. Singh, and K. K. Mohanty, SPE J. **7**, 40 (2002).

[35] M. S. Talukdar and O. Torsaeter, J. Pet. Sci. Eng. **33**, 265 (2002); M. S. Talukdar, O. Torsaeter, M. A. Ioannidis, and J. Howard, *ibid.* **35**, 1 (2002); Transp. Porous Media **48**, 101 (2002).

[36] P. Čapek, V. Hejtmánek, L. Brabec, A. Zikánová, and M. Kočiřik, Transp. Porous Media **76**, 179 (2009); P. Čapek, V. Hejtmánek, J. Kolafa, and L. Brabec, *ibid.* **88**, 87 (2011).

[37] J. Serra, *Image Analysis and Mathematical Morphology* (Academic Press, London, 1982).

[38] S. Torquato and B. Lu, Phys. Rev. E **47**, 2950 (1993).

[39] I. Cousin, P. Levitz, and A. Bruand, Eur. J. Soil Sci. **47**, 439 (1996).

[40] A. P. Roberts and S. Torquato, Phys. Rev. E **59**, 4953 (1999).

[41] H. Hamzehpour and M. Sahimi, Phys. Rev. E **74**, 026308 (2006); H. Hamzehpour, M. R. Rasaei, and M. Sahimi, *ibid.* **75**, 056311 (2007).

[42] Y. Jiao, F. H. Stillinger, and S. Torquato, Proc. Natl. Acad. Sci. U.S.A. **106**, 17634 (2009); C. E. Zachary and S. Torquato, Phys. Rev. E **84**, 056102 (2011).

[43] P. Tahmasebi, A. Hezarkhani, and M. Sahimi, Comput. Geosci. **16**, 779 (2012).

[44] S. Strebelle, Math. Geol. **34**, 1 (2002).

[45] H. Okabe and M. J. Blunt, Phys. Rev. E **70**, 066135 (2004); J. Pet. Sci. Eng. **46**, 121 (2005).

[46] A. Hajizadeh, A. Safekordi, and F. A. Farhadpour, Adv. Water Resour. **34**, 1256 (2011).

[47] L. Di Stefano, S. Mattoccia, and F. Tombari, Pattern Recog. Lett. **26**, 2129 (2005).

[48] F. Höppner and F. Klawonn, in Proceedings of the 8th International Symposium on Intelligent Data Analysis, Advances in Intelligent Data Analysis VIII, 2009 (unpublished), p. 71.

[49] C. Daly, in *Geostatistics*, edited by O. Leuangthong and C. V. Deutsch (Springer, New York, 2004), p. 215; A. El Ouassini, A. Saucier, D. Marcotte, and B. Favis, Chaos Solitons Fractals **36**, 418 (2008); G. Mariethoz, P. Renard, and J. Straubhaar, Water Resour. Res. **46**, W11536 (2010).

[50] C. E. Shannon, Bell Syst. Tech. J. **27**, 379 (1948).

[51] [http://www3.imperial.ac.uk/earthscienceandengineering/research/perm/porescalemodeling].

[52] S. Krishna and A. G. Journel, Math. Geol. **35**, 915 (2003).

[53] C. V. Deutsch, FLOWSIM: [http://www.ualberta.ca/∼cdeutsch].

[54] H. Dong and M. J. Blunt, Phys. Rev. E **80**, 036307 (2009).

[55] P. H. Valvatn and M. J. Blunt, Water Resour. Res. **40**, W07406 (2004).